Cardiac PET/MR Basics

2

Yoann Petibon, Chao Ma, Jinsong Ouyang, and Georges El Fakhri

Introduction

Hybrid positron emission tomography (PET) and magnetic resonance (MR) (PET/MR) is rapidly gaining momentum as a powerful imaging modality for both clinical and basic research applications. The first clinical whole-body PET/MR systems were FDA-cleared and installed in 2010. Since then, the number of systems in use worldwide has grown steadily, with ~260 fully integrated PET/MRs installed globally at the end of 2020 (Fig. 2.1a). The expanding base of installed scanners in the last decade has been accompanied with very active research, both fundamental and clinical, with over 4250 articles referencing PET/MR by the end of 2020 (Fig. 2.1b). At its most basic level, PET/MR combines the strengths of each modality, enabling imaging of physiology with the exceptional molecular sensitivity of PET complemented with the high-resolution structural information of MRI and its multitude of complementary functional (e.g., perfusion) and molecular (e.g., spectroscopy) measurements. Besides the superior soft-tissue contrast of MRI as compared to computed tomography (CT) as well as its unique ability to probe tissue composition, the use of MRI as the anatomical complement to PET comes with the benefit of a lower effective radiation exposure in PET/MR as compared to PET/CT, which is a significant advantage for pediatric applications and protocols that require serial imaging, e.g., for staging and monitoring response to therapy. Furthermore, the intrinsic spatial and temporal alignment of PET and MR data in fully integrated PET/MR machines can be exploited to perform MR-based motion correction of PET [1] and anatomically guided PET reconstruction [2] for partial volume effect correction and noise control, yielding substantial improvements in PET image quality and accuracy. Last but not least, simultaneous PET/MR offers opportunities to quantify physiological processes that would otherwise be difficult to assay with either modality alone as demonstrated in cardiac imaging with quantitative mapping of mitochondrial membrane potential using a voltage-sensitive PET tracer and MRI-based measurement of myocardial extracellular volume fraction [3–5].

PET/MR has been the subject of active interdisciplinary research aimed at developing solutions for many of the physical (e.g., instrumentation) and practical (e.g., attenuation correction) challenges associated with this hybrid imaging modality. Furthermore, thorough research has been undertaken to take full advantage of the unique opportunities (e.g., motion correction) of this imaging technique in specific clinical applications. The aim of this chapter is to

Y. Petibon · C. Ma · J. Ouyang · G. El Fakhri (✉)
Gordon Center for Medical Imaging, Department of Radiology, Harvard Medical School, Massachusetts General Hospital, Boston, MA, USA
e-mail: elfakhri.georges@mgh.harvard.edu

© The Author(s), under exclusive license to Springer Nature Switzerland AG 2022

M. Pelletier-Galarneau, P. Martineau (eds.), *FDG-PET/CT and PET/MR in Cardiovascular Diseases*, https://doi.org/10.1007/978-3-031-09807-9_2

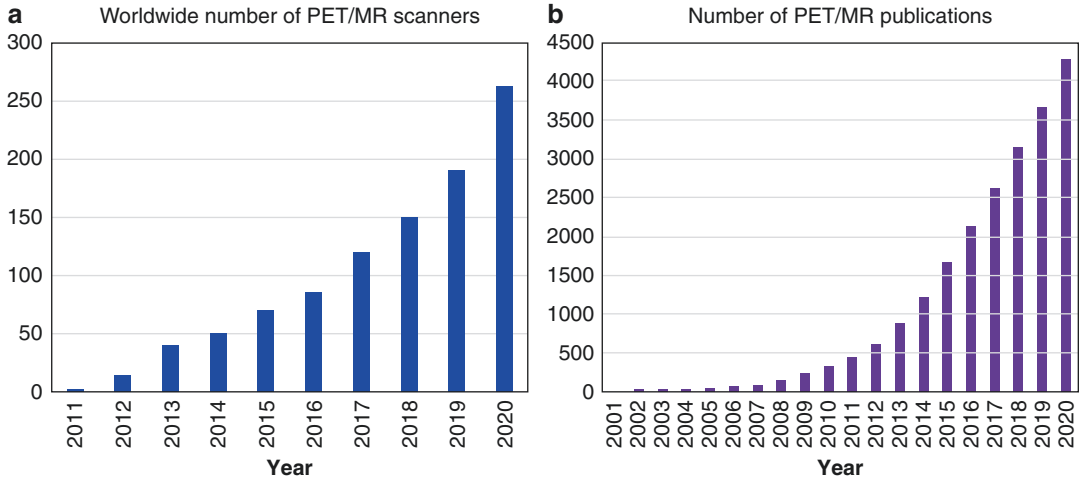

Fig. 2.1 (**a**) Number of PET/MR scanners installed worldwide. (Source: Siemens Healthineers, GE Healthcare, United Imaging). (**b**) Number of PET/MR publications. (Source: PubMed)

provide a brief overview of the challenges and opportunities associated with PET/MR, with a particular emphasis given to cardiac imaging applications. We also briefly present current clinical applications as well as future directions in cardiac MR imaging in the context of PET/MR.

PET/MR Instrumentation

The integration of PET and MRI scanners into a single machine represents a significant engineering achievement owing to the mutual interferences and crosstalk between the two systems [6, 7]. Indeed, all components needed for the formation and acquisition of MR signals (e.g., static main magnetic field (B0), radiofrequency field (B1), and gradient fields) can affect the normal operation of standard PET detectors and electronics, therefore necessitating the development of specific MRI compatible instrumentation for combined PET/MR scanners. For example, the photomultiplier tubes (PMTs) that had traditionally been used in PET detectors for signal amplification cannot be operated in the presence of even small magnetic fields, as electromagnetic forces perturb the movement of electrons down the chain of dynodes in the PMT and significantly impair its amplification power [6]. Integrated PET/MR scanners instead rely on a different type of photodetector technologies such as avalanche photodiodes (APDs) [8] or silicon photomultipliers (SiPMs) [9], which are largely insensitive to magnetic fields. Likewise, the introduction of PET instrumentation (e.g., scintillation crystals, electronics, shielding) into the bore of the magnet can affect MRI data acquisition by distorting the B_0 and B_1 fields and the linearity of the gradient fields, resulting in image artifacts. For example, PET scintillation crystals that contain gadolinium such as LGSO (lutetium gadolinium orthosilicate) are not suitable for use in PET/MR due to their high magnetic susceptibility [10]. Hybrid PET/MR systems thus employ detectors made with materials such as lutetium-yttrium oxyorthosilicate (LYSO). There are also physical constraints associated with integrating a PET scanner within an MRI gantry since the two systems have outer bores in the range of ~1 m diameter, requiring the PET instrumentation to be very compact in order to fit into the bore. In this regard, APDs and SiPMs are not only MRI compatible but also much less voluminous than PMTs and therefore represent a particularly well-suited technology for PET/MR. Nevertheless, combined PET/MR systems all have narrow bores (about 60 cm diameter), which can cause practical difficulties for studying large or claustrophobic patients.

Four clinical whole-body (WB) PET/MR scanners have been introduced commercially so far. The first WB PET/MR machine was released by Philips Healthcare in 2010 with the TF

Ingenuity [11]. Unlike the systems that followed, the TF Ingenuity PET/MR allowed for sequential—as opposed to simultaneous—PET and MRI scanning, with each system physically separated from the other to minimize interferences, and a rotating bed shuttling the patient between the two gantries. In spite of the physical separation between the two scanners, magnetic shielding still had to be introduced within the design of the PET scanner to allow its detectors—based on conventional PMTs and LYSO crystals (size: 4 ×4 ×22 mm^3)—to properly function. Shortly after, Siemens Healthcare introduced the Biograph mMR, the first fully integrated WB system capable of simultaneous PET and MR acquisition [12]. The Biograph mMR is a hybrid PET/MR system consisting of a 3-T whole-body MRI scanner and a PET gantry installed between the gradient and body coils. The PET detector system employs lutetium oxyorthosilicate (LSO) scintillators (4 ×4 ×20 mm^3) coupled with APD arrays and allows an axial coverage of 25.8-cm, compared to the 18-cm axial FOV of the Ingenuity TF. In 2015, General Electric (GE) released the Signa PET/MR [13, 14] the first integrated PET/MR machine with time-of-flight (TOF) capability. The MRI component of the Signa is based on 3-T Discovery 750w MRI platform and the PET detector system employs lutetium-based scintillators ("LBS," size: 3.95× 5.3× 25 mm^3) coupled to SiPMs, offering a 394 ps TOF timing resolution and a 25 cm axial FOV [14]. The uPMR 790 is another integrated TOF PET/MR system recently introduced by United Imaging Healthcare [15]. The scanner comprises a 3-T superconducting magnet and a PET system consisting of LYSO crystals (size: 2.76× 2.76× 15.5 mm^3) also coupled with SiPMs. The system has a timing resolution at ~540 ps [15] and its axial field of view is 32 cm long, the largest among all currently available commercial PET/MR scanners.

As mentioned above, all integrated clinical WB PET/MR scanners rely on solid-state photodetectors such as APDs or SiPMs. Both devices are silicon semiconductor photodetectors, based on a modified p-n junction with an external bias voltage applied for charge carrier acceleration [9]. Because the distances traveled by the charges in the APD and SiPM are small, these photodetectors are largely insensitive to magnetic fields [6, 16, 17]. Though APDs are MRI compatible and highly compact, their amplification performance strongly depends on the temperature and the strength of the applied voltage [6], which requires very tight control of these parameters for stable operation. Furthermore, APDs have a much lower gain than conventional PMTs as well as a poor timing resolution, precluding measurement of photon TOF. The SiPM is an alternative photodetector technology consisting of a 2-D array of thousands of APDs operated in Geiger mode (i.e., with a bias voltage higher than the breakdown voltage). In the SiPM, each Geiger APD within the detector array effectively operates as a single photon counter and is processed independently and simultaneously with the other ones [6, 9]. SiPMs have a very high gain, equivalent or higher than that of conventional PMTs, as well as an excellent timing resolution, which enables TOF measurement.

Attenuation Correction

Attenuation correction (AC) is critical to obtain quantitatively accurate PET images. Until the introduction of hybrid PET/computed tomography (CT) systems in the early 2000s, standalone PET cameras employed rotating positron-emitting transmission sources to directly measure attenuation of annihilation photons. In PET/CT scanners, attenuation maps are derived from low-dose CT images by exploiting the linear relationships that exist between CT Hounsfield units (HU) and attenuation coefficients at 511 keV [18]. However, none of the commercially available PET/MR systems is equipped with a CT gantry or a transmission source, meaning that attenuation maps must be obtained from MR images [19, 20]. Generating accurate MR-based attenuation maps for human tissues is technically very challenging as there is no direct relationship between the tissue properties measured by MRI (e.g., proton density, relaxation times) and the underlying electron densities which determine the linear attenuation coefficients. For instance, tissues such as bone and lung exhibit drastic dif-

ferences in the degree to which they attenuate annihilation photons, yet both show very low MRI signals when imaged by conventional pulse sequence because of their ultra-short T_2* relaxation times (<1 ms) and low proton densities.

MR-based AC (MRAC) in PET/MR has been the subject of extensive research and several approaches have been investigated. The most widely used MRAC method consists in segmenting MR images of the subject into different tissue classes and then to assign a discrete attenuation coefficient to each tissue type [19, 20]. The most commonly used segmentation-based MRAC method relies on a fast 3D two-point Dixon acquisition for water/fat separation. The acquired in-phase and out-phase images are then used to generate piecewise constant PET attenuation maps with four compartments: air, lung, fat and non-fat soft tissue [19]. Though widely used in PET/MR scanners, this approach has several limitations, the principal one being that it incorrectly assigns the attenuation coefficient of soft tissue to cortical bones. This underestimation of attenuation effects introduces substantial quantitation errors within the bones themselves and in tissues located in their vicinity [21, 22] (Fig. 2.2).

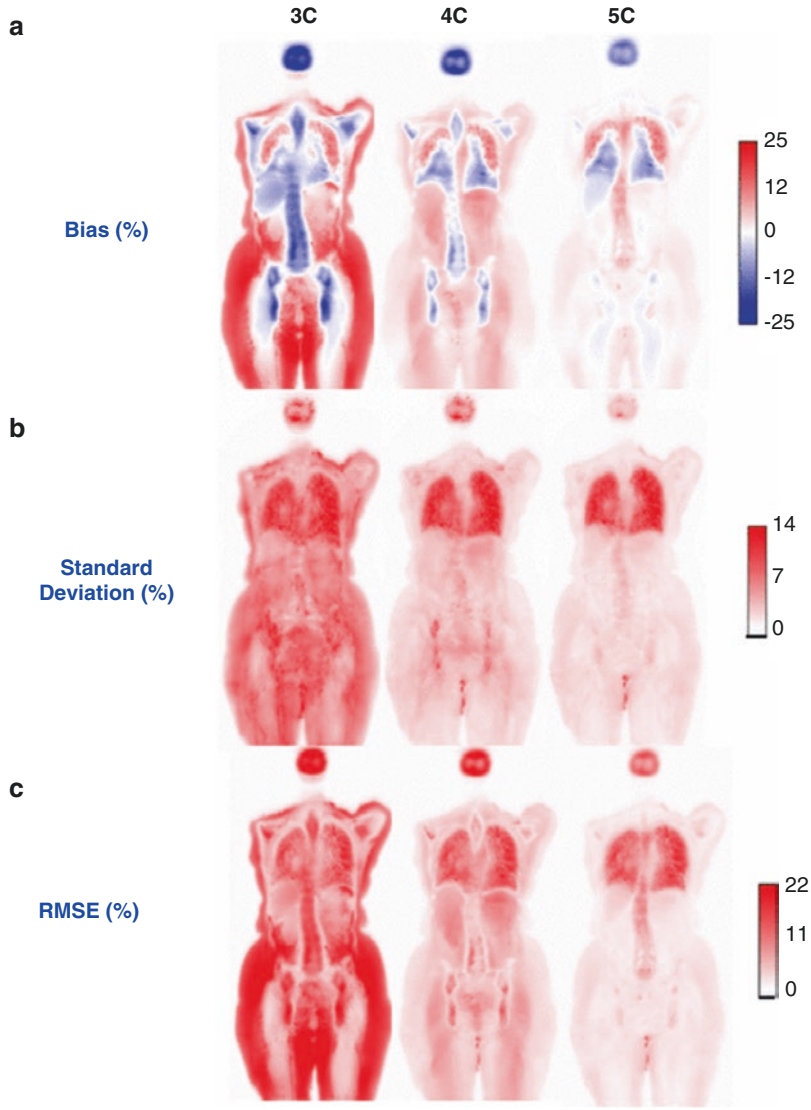

Fig. 2.2 Whole-body atlases of mean (**a**), standard deviation (**b**), and root mean-squared error ("RMSE," **c**) ^{18}F-FDG SUV bias computed based on 23 patient data sets for different segmentation-based attenuation correction methods. 3-classes ("3C": air, lung, soft-tissue), 4-classes ("4C": air, lung, fat, non-fat soft-tissue), and 5-classes ("5C": air, lung, fat, non-fat soft-tissue, bone) attenuation maps. (Reproduced from [24], with permission)

Besides bones, tissue misclassification errors have been reported in other body locations such as the bronchus, causing further image artifacts [23]. Nevertheless, the bias in activity estimates reported within soft tissue organs such as the heart, liver, and kidney remains relatively small with these approaches, in the range of a few percent typically [24]. To obtain bone information for MRAC, methods leveraging special pulse sequences with very short echo times such as UTE (ultrashort-echo-time), ZTE (zero-echo-time), or combination of UTE/ZTE with Dixon acquisitions have been investigated in brain [25–28] and pelvic [29] imaging applications. However, these approaches come at the price of longer acquisition times and often require some level of human intervention, e.g., during bone segmentation [29]. A second type of approach to MRAC generates attenuation maps that can account for bones by registering image data from individual subjects to pre-computed attenuation atlases/templates, as shown in brain [30–32] and whole-body [33] imaging. These methods have been found to offer accurate results in the brain [34]; however, their application in body imaging remains challenging due to the larger subject-to-subject variability in terms of anatomy, body mass index, and/or disease [35]. Furthermore, atlas-based methods are intrinsically limited in their ability to account for subject-specific variations in bone density and structure. A third category of MRAC techniques employs machine learning to synthesize pseudo-CT distributions from MR images in a fully automated fashion [36–40] (Fig. 2.3). These methods usually rely on deep convolutional neural networks (CNNs) to learn a nonlinear mapping between input MRI data (e.g., Dixon data only [36, 40], Dixon-ZTE [37], multi-echo Dixon/UTE [38]) and ground-truth CT attenuation during a training step, using patch- [37] or slice-based [36, 38] approaches. CNNs are a specific kind of artificial neural net-

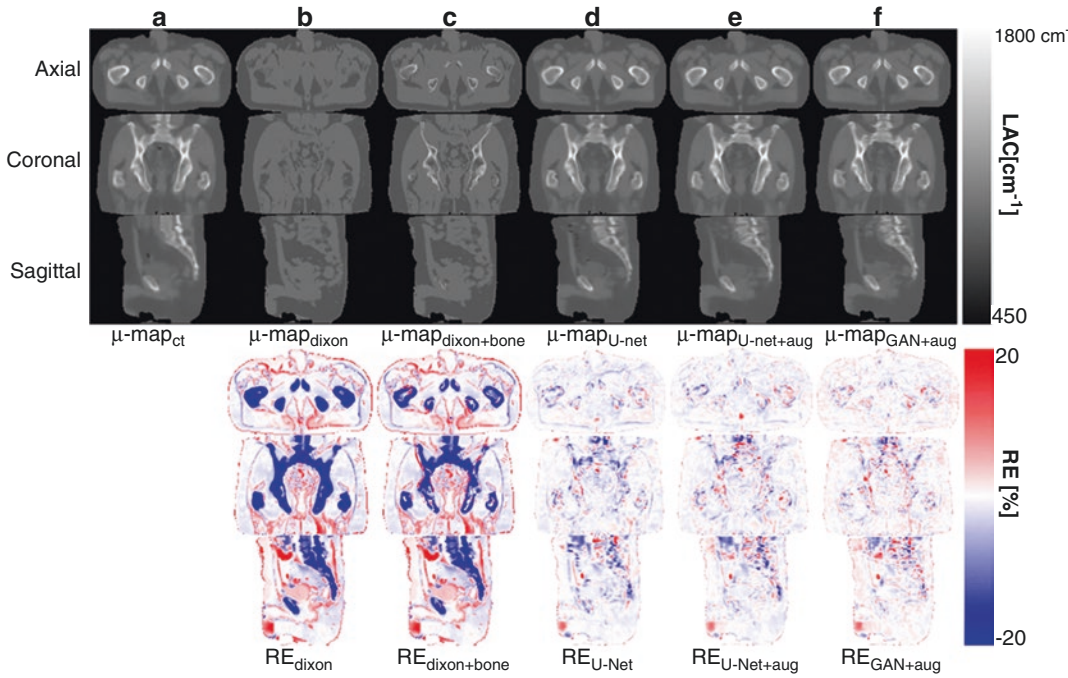

Fig. 2.3 Comparison of attenuation maps in the pelvic region obtained using (**a**): CT (μ-map$_{CT}$); (**b**): the standard Dixon MRI-based method (μ-map$_{dixon}$), (**c**): Dixon MRI with atlas-based bone information (μ-map$_{dixon\ +\ bone}$); and (**d–f**): deep learning based algorithms (μ-map$_{U\text{-}net}$, μ-map$_{U\text{-}net\ +\ aug}$, and μ-map$_{GAN\ +\ aug}$). Overall, there is excellent correlation between CT and the different deep-learning approaches. The lower panel displays images of relative differences between the different attenuation maps and the reference CT. (Reproduced from [40], with permission)

works specialized for the analysis of image data. Deep CNNs typically operate by applying a series of filtering and down/upsampling operations designed to extract the most relevant features of the input data for the task at hand. The parameters of the deep CNN (e.g., filters' coefficients) are learned during a training phase in which a cost-function measuring the discrepancy between outputs of the deep CNN (e.g., "pseudo-CT" image) and the labels (e.g., ground-truth CT image) is minimized. Deep learning based MRAC algorithms have been shown to provide accurate results in the pelvis [36, 37, 40] and brain [38, 39], typically within a few percent of the reference CT-based results. However, their performance has yet to be fully evaluated in large patient cohorts.

The challenge of attenuation correction in PET/MR is further complicated by the so-called truncation artifacts [20]. Indeed, the transaxial FOV of MRI is usually restricted to a sphere of 25 cm radius around the isocenter where the B0 field has the best uniformity, meaning that attenuating tissues positioned toward the edges of the bore cannot be imaged accurately and display severe geometric distortions or even signal voids and truncation [41]. For instance, thoracic PET/MR studies with arms-down often truncate the MR signal from the arms, complicating the estimation of attenuation effects from the truncated tissues. If uncorrected, truncation artifacts in the attenuation maps can lead to bias in the reconstructed activity distributions that extend well beyond the missing tissues. Different methods have been developed to address this problem. PET-based approaches, such as maximum likelihood estimation of activity and attenuation (MLAA) [42, 43], seek to estimate body contours from the emission data themselves. However, the quality of MLAA-based correction depends on the type of tracer used and inaccurate results have been reported with tracers that show low accumulation in the extremities such as ^{68}Ga-PSMA [41]. MR-based methods for truncation correction include "B0 Homogenization Using Gradient Enhancement" (HUGE) [41, 44], which effectively extends the MR FOV beyond its traditional limits. Unlike MLAA, this approach is agnostic to the radiotracer used during the study and was found to provide more robust performance than (non-TOF) MLAA-based methods across different tracers [41].

Finally, PET/MR scanning of the body often requires the use of flexible radiofrequency (RF) surface coils for MR data acquisition, which are made of various materials such as plastic and rubber as well as high attenuating components such as the hardware used for electronic circuitry [45]. These RF coils are located in the PET FOV during the acquisition but are not accounted for by current attenuation correction schemes since their position and individual geometries are in practice unknown in whole-body scans. Studies have reported PET count losses in the range of 2–5% due to these flexible RF coils and substantial underestimation of the reconstructed activity concentration in the vicinity of the high attenuating electronic hardware components [46].

Motion Correction

Signal-to-noise ratio (SNR) in PET primarily depends on the number of coincidence events acquired during the scan. Consequently, acquisition times typically extend over several minutes for each bed position (and even up to 1 or 2 h for some dynamic studies), making PET particularly susceptible to patient movement, both involuntary (e.g., respiration and cardiac contractions) and voluntary (e.g., body motion). Cardiac PET studies are especially subject to motion effects as the heart undergoes the simultaneous action of respiratory motion, shifting the heart by more than 1 cm along the superior–inferior direction [47], and cardiac contractions, moving the base of the heart toward the apex by an average of ~12 mm [48] while thickening the wall by ~4–6 mm [49]. In addition to these pseudo-cyclic physiologic displacements, subjects may move in a completely unpredictable manner during the PET scan, e.g., due to discomfort, pain, coughing, or deep breathing, and such body movements are more likely to occur during longer acquisitions, e.g., dynamic PET studies. The continuous motion of organs during scanning introduces arti-

facts that alter quantification of tracer concentration in moving tissues and deteriorate the diagnostic quality of PET images. Two types of image artifacts result from motion. One presents as a spatially dependent smearing (or blurring) of the reconstructed activity distributions, reducing the effective PET spatial resolution and introducing errors in estimates of local radioactivity concentration. The other stems from spatial inconsistencies between the attenuation map—acquired during a breath-hold in standard PET/CT and PET/MR protocols—and the emission data, which can be treated as acquired at an average position over many motion phases, cardiac/respiratory cycles, and body poses. Motion-induced emission/attenuation discrepancies can introduce severe image artifacts primarily in regions adjacent to large attenuation gradients (e.g., heart/lung and liver/lung interfaces), deteriorating the diagnostic value of PET [50, 51].

Integrated PET/MR systems are uniquely capable of providing an accurate and robust solution to the motion problem in PET [1, 52–57]. Indeed, owing to its lack of ionizing radiation, excellent soft-tissue contrast, high SNR, and very good spatiotemporal resolution, MRI has ideal characteristics for measuring organ motion. Furthermore, because of the simultaneity and inherent alignment between the two modalities, MRI-derived motion information can be leveraged to compensate motion effects in PET images. MR-based motion correction of PET has been investigated extensively in recent years, with applications in imaging of the brain [58, 59], thoracic or abdominal malignancies [60–69], and heart [64, 70–79].

MR-based PET motion correction approaches are generally quite complex, involving a coordinated set of MR sequences, PET acquisitions, and data postprocessing steps that often need to be customized depending on the targeted body region (e.g., brain vs. heart) and the type of motion to be corrected (e.g., physiologic vs. bulk motion) [55]. Figure 2.4 presents a general PET/MR data acquisition and processing pipeline for cardiac/respiratory motion correction. The first step is a PET/MR scan involving the acquisition of an attenuation map followed by a special pulse sequence designed to capture organ motion during PET data acquisition in list mode, in which each coincidence event is recorded as to its time of acquisition. Motion measurement sequences are usually customized for capturing the specific motion of the organ or body region of interest. For instance, tagged MRI [80] can be employed to measure contractile motion of the myocardium [81, 82] but it is not practical to use tagging for measuring respiratory motion of the heart as tag patterns fade more rapidly than a typical respiratory cycle. Alternatively, T2-prepared bright blood MRI sequences might be better suited for measuring heart respiratory displacements [77]. Another critical aspect of the PET/MR acquisition scheme pertains to the tracking of motion phases as a function of scan time, such that each coincidence event and MR k-space readout can be gated, i.e., assigned a specific motion phase. Cardiac motion phase tracking can be achieved quite robustly with electrocardiogram (ECG) devices. For respiratory motion, phase tracking can be performed via 1-D navigator echoes [63, 83] or low-resolution 2-D image navigator modules [69, 77] inserted in the motion measurement sequence, or using respiratory bellows or list-mode PET-driven signals [62, 81, 84]. Phase tracking signals are then used to construct motion-resolved MR volumes, i.e., 3D images of the subject's anatomy in the different motion instants, and to bin the PET coincidence events into the different phases. The next step is motion estimation which is typically performed by registering the MR volumes from the different phases to a reference one, although some groups have also investigated registration algorithms that make use of both PET and MR images [79]. This step produces motion vector fields (i.e., dense sets of 3D displacements), describing the voxel-to-voxel spatial coordinate correspondence between each motion phase and the reference phase. A motion-dependent attenuation map can then be synthesized by applying the estimated motion vector fields to the acquired attenuation map after aligning it to the reference MR volume to compensate for potential discrepancies. At last, the motion fields and motion-dependent attenuation maps can be integrated within itera-

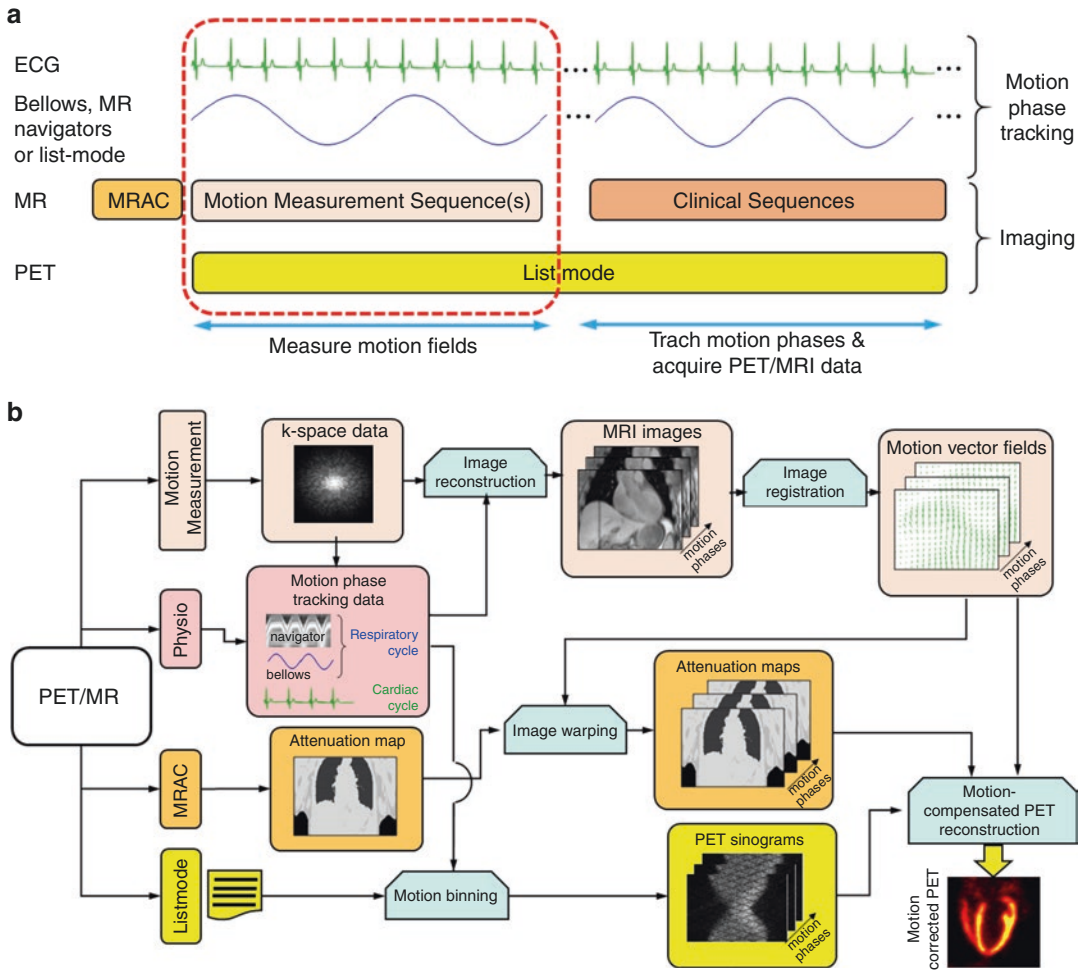

Fig. 2.4 Schematic representation of PET/MR data acquisition (**a**) and processing pipeline (**b**) for MR-based motion correction of PET

tive PET reconstruction [85, 86] to correct motion effects. An alternative approach that is also easier to implement is to independently reconstruct each gated PET volume using standard algorithms and then to apply the estimated motion fields to align them to the reference phase, followed by averaging of the resulting images. Figure 2.5 illustrates the impact of MR-based PET motion correction in myocardial perfusion imaging [82] using ^{18}F-flurpiridaz [87].

It is worth noting that the pulse sequences used for motion field measurement are usually not part of the diagnostic MR protocol and clinical sequences are thus played either before or after these acquisitions. In theory, it is possible to make use of the PET data acquired during diagnostic MR imaging for motion correction by continuing the acquisition of motion phase tracking signals as illustrated in Fig. 2.4a. As for respiratory motion phase tracking, while it is technically possible to incorporate MR navigators into clinical pulse sequences, modifying every sequence across all manufacturers is impractical; additionally, navigator acquisitions can interfere with the normal operation of other sequences. A more practical approach is to rely on external sensors or methods that do not interfere with the MR or PET acquisition such as respiratory bellows or list-mode driven respiratory gating [84].

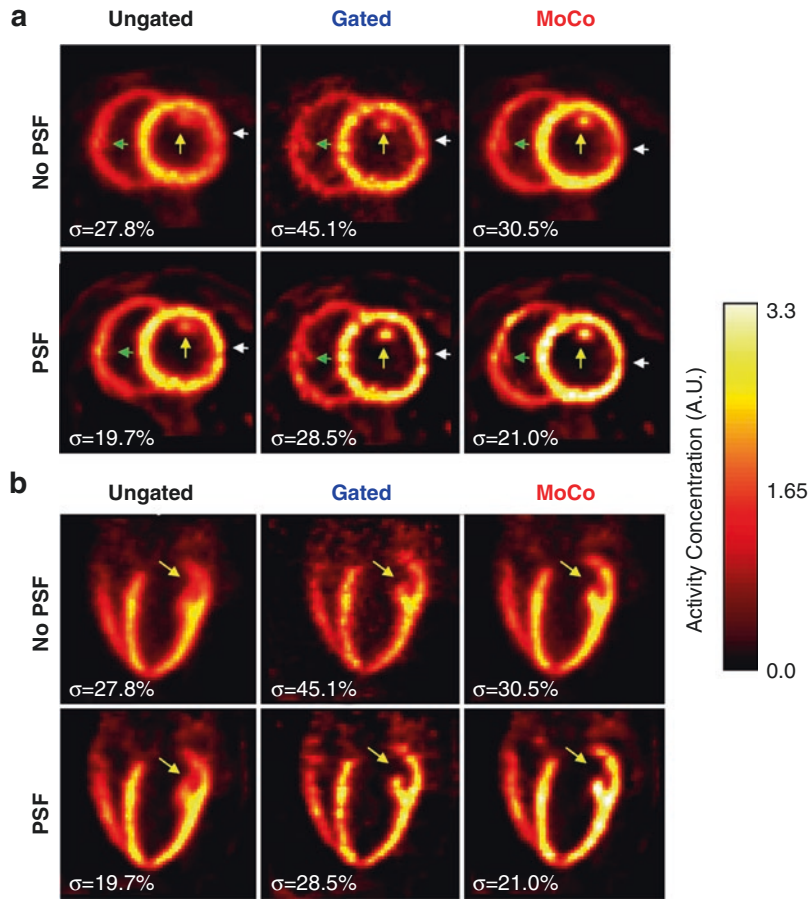

Fig. 2.5 Impact of motion and point spread function (PSF) correction in ^{18}F-Flurpiridaz PET/MR myocardial perfusion imaging (swine model). (**a**) and (**b**), respectively, show short- and long-axis PET images reconstructed without motion correction ("Ungated"), cardiac gating ("Gated," end-diastole), and motion correction ("Moco") based on a tagged MRI acquisition, each without and with PSF modeling. MR-based motion correction leads to higher image resolution as evidenced by improved visibility of the papillary muscles as compared to no motion correction. (Reproduced from [82], with permission)

Owing to the unpredictability of body motion, its tracking and measurement using MRI would effectively require playing a dedicated structural (or navigator) sequence continuously during the PET acquisition [88]. An alternative and arguably more practical strategy is to rely on PET-driven methods [89–91]. One possible approach is to divide the PET list-mode data into temporal frames of relatively short duration (a few seconds, typically) and then to reconstruct the data in each frame using ultra-fast list-mode based reconstruction algorithms [89]. The resulting images can then be used to determine motion fields between each frame and a selected reference one using image registration. In cases where the activity distribution changes rapidly, during a dynamic study, for instance, registration can be performed between temporally adjacent frames to improve motion estimation. Note that the same approach could be used to account for both body and respiration motion if very short time frames (e.g., <1 s) are employed, although PET image noise may degrade the performance of motion estimation and correction. An alternative PET-driven strategy for body motion correction consists in computing the coordinates of the activity distribution's center of mass ("COM") [91] or center of detection [90] ("COD"—if TOF is available) from the list-mode data as a function of scan time. Analysis of the extracted traces can then be used to detect motion under the assumption that body movements cause abrupt changes in COM or COD coordinates. List-mode scan data can then be parsed into frames accordingly, reconstructed and registered for motion estimation and correction [90, 91].

Radiation Dose Reduction

PET/MRI offers a substantially reduced radiation exposure compared with PET/CT owing to the elimination of CT and the associated radiation dose from the patient workup. For whole body examinations, a potential reduction in effective radiation exposure of up to 80% can be achieved with PET/MRI relative to standard PET/CT [92–94]. This represents a significant benefit for children and young adult populations considering the cumulative dose associated with multiple examinations, e.g. for staging, therapy monitoring, and follow-up, and the risk of developing secondary malignancies later in life due to radiation exposure [95, 96]. Furthermore, with MR acquisition protocols generally requiring longer time per bed position, it may also be possible to further reduce the injected tracer dose in PET/MR examinations [95].

Cardiac MRI

Because of its high spatial and temporal resolution and excellent soft-tissue contrast, cardiac MRI is recognized as the reference method for myocardial tissue characterization and ventricular function assessment, providing structural and functional information of the heart complementary to the molecular information from PET [97]. Conventional T1- and T2-contrast weighted cardiac MR sequences, such as late gadolinium enhancement (LGE) and fast spin-echo (FSE), provide qualitative assessment of the myocardium but are limited in their ability to detect and grade diffuse diseases. Cardiac parametric mapping methods, including T1, T2, and T2* mapping, can address these limitations by providing quantitative characterization of myocardial tissue composition [98]. The longitudinal relaxation time (T1) characterizes alterations in the structure and intra/extracellular components of the myocardium. Modified Look-Locker inversion recovery (MOLLI) is a widely used method for cardiac T1 mapping [99]. It utilizes inversion recovery (IR) pulses followed by ECG-gated balanced steady-state free precession (bSSFP) acquisitions over multiple cardiac cycles to allow estimation of myocardial T1 in a single breath-hold. A variety of inversion- and/or saturation-recovery schemes have been developed to improve the accuracy of T1 mapping [100]. The extracellular volume fraction (ECV), measured from pre- and post-contrast T1 values, is an emerging biomarker for diffuse fibrosis, e.g., in heart failure, dilated cardiomyopathy, and amyloidosis, which is known to be particularly challenging to detect using the conventional LGE method [98]. The transverse relaxation time (T2) is sensitive to changes in water content of the myocardium, e.g. in presence of edema [101]. In cardiac T2 mapping, T2 preparation modules with different durations are inserted in each cardiac cycle followed by ECG-gated bSSFP or spoiled gradient echo (GRE) acquisitions with breath-holding [98]. The T2* relaxation time reflects the decay of the transverse magnetization in the presence of local B0 field inhomogeneity and is used for assessment of myocardial iron load. Cardiac T2* mapping is often performed using ECG-gated GRE acquisitions at different echo times with breath-holding [98]. Finally, cardiac cine MR imaging is the gold standard approach to assessing ventricular function, including ejection fraction, myocardial mass, and myocardial wall motion [102].

All current commercial PET/MR scanners operate at 3 T. Compared to 1.5 T, cardiac MR at 3 T faces several unique challenges. Due to the more severe B0 inhomogeneity at 3 T, sequences using bSSFP acquisitions are prone to the well-known banding artifacts, imposing challenges in B0 shimming and preventing from 3D cardiac imaging. In addition, transmit B1 variations on the order of 30–60% over the left ventricle have been reported [103], causing bias in the estimated T1 values at 3 T. Besides the above hardware-related challenges, cardiac and respiratory motions cause significant difficulties in cardiac MR. As a result, commercially available cardiac parametric mapping sequences are 2D imaging sequences with breath-holding acquisitions, which limit both the resolution and spatial coverage in the slice selective direction. Furthermore, acquiring multiple parametric maps (T1, T2, etc.)

prolongs the total imaging time. Therefore, very active research efforts are being undertaken to achieve 3D, high-resolution, multi-parametric cardiac imaging with free-breathing or even ECG-gating free acquisitions, including respiratory and cardiac gating-based free-breathing methods [104], sparse sampling methods with constrained image reconstruction [105, 106], MR multitasking [107], and MR fingerprinting [108].

References

1. Ouyang J, Li Q, El Fakhri G. Magnetic resonance-based motion correction for positron emission tomography imaging. Semin Nucl Med. 2013;43(1):60–7. https://doi.org/10.1053/j.semnuclmed.2012.08.007.
2. Bai B, Li Q, Leahy RM. Magnetic resonance-guided positron emission tomography image reconstruction. Semin Nucl Med. 2013;43(1):30–44. https://doi.org/10.1053/j.semnuclmed.2012.08.006.
3. Alpert NM, et al. Quantitative in vivo mapping of myocardial mitochondrial membrane potential. PLoS One. 2018;13(1):e0190968.
4. Pelletier-Galarneau M, et al. In vivo quantitative mapping of human mitochondrial cardiac membrane potential: a feasibility study. Eur J Nucl Med Mol Imaging. 2021;48(2):414–20. https://doi.org/10.1007/s00259-020-04878-9.
5. Alpert NM, et al. In-vivo imaging of mitochondrial depolarization of myocardium with positron emission tomography and a proton gradient uncoupler. Front Physiol. 2020;11:11–491. https://doi.org/10.3389/fphys.2020.00491.
6. Vandenberghe S, Marsden PK. PET-MRI: a review of challenges and solutions in the development of integrated multimodality imaging. Phys Med Biol. 2015;60(4):R115–54. https://doi.org/10.1088/0031-9155/60/4/R115.
7. Delso G, Ziegler S. PET/MRI system design. Eur J Nucl Med Mol Imaging. 2009;36(S1):86–92. https://doi.org/10.1007/s00259-008-1008-6.
8. Renker D. New trends on photodetectors. Nucl Instrum Methods Phys Res Sect Accel Spectrometers Detect Assoc Equip. 2007;571(1–2):1–6. https://doi.org/10.1016/j.nima.2006.10.016.
9. Roncali E, Cherry SR. Application of silicon photomultipliers to positron emission tomography. Ann Biomed Eng. 2011;39(4):1358–77. https://doi.org/10.1007/s10439-011-0266-9.
10. Yamamoto S, Kuroda K, Senda M. Scintillator selection for MR-compatible gamma detectors. IEEE Trans Nucl Sci. 2003;50(5):1683–5. https://doi.org/10.1109/TNS.2003.817375.
11. Zaidi H, et al. Design and performance evaluation of a whole-body ingenuity TF PET–MRI system. Phys Med Biol. 2011;56(10):3091–106. https://doi.org/10.1088/0031-9155/56/10/013.
12. Delso G, et al. Performance measurements of the Siemens mMR integrated whole-body PET/MR scanner. J Nucl Med. 2011;52(12):1914–22. https://doi.org/10.2967/jnumed.111.092726.
13. Grant AM, Deller TW, Khalighi MM, Maramraju SH, Delso G, Levin CS. NEMA NU 2-2012 performance studies for the SiPM-based ToF-PET component of the GE SIGNA PET/MR system: PET performance measurements of the GE SIGNA PET/MR. Med Phys. 2016;43(5):2334–43. https://doi.org/10.1118/1.4945416.
14. Levin CS, Maramraju SH, Khalighi MM, Deller TW, Delso G, Jansen F. Design features and mutual compatibility studies of the time-of-flight PET capable GE SIGNA PET/MR system. IEEE Trans Med Imaging. 2016;35(8):1907–14. https://doi.org/10.1109/TMI.2016.2537811.
15. Chen S, et al. NEMA NU2-2012 performance measurements of the united imaging uPMR790: an integrated PET/MR system. Eur J Nucl Med Mol Imaging. 2021;48(6):1726–35. https://doi.org/10.1007/s00259-020-05135-9.
16. Pichler BJ, et al. Performance test of an LSO-APD detector in a 7-T MRI scanner for simultaneous PET/MRI. J Nucl Med. 2006;47(4):639–47.
17. España S, Fraile LM, Herraiz JL, Udías JM, Desco M, Vaquero JJ. Performance evaluation of SiPM photodetectors for PET imaging in the presence of magnetic fields. Nucl Instrum Methods Phys Res Sect Accel Spectrometers Detect Assoc Equip. 2010;613(2):308–16. https://doi.org/10.1016/j.nima.2009.11.066.
18. Kinahan PE, Hasegawa BH, Beyer T. X-ray-based attenuation correction for positron emission tomography/computed tomography scanners. Semin Nucl Med. 2003;33(3):166–79. https://doi.org/10.1053/snuc.2003.127307.
19. Martinez-Möller A, et al. Tissue classification as a potential approach for attenuation correction in whole-body PET/MRI: evaluation with PET/CT data. J Nucl Med. 2009;50(4):520–6. https://doi.org/10.2967/jnumed.108.054726.
20. Keereman V, Mollet P, Berker Y, Schulz V, Vandenberghe S. Challenges and current methods for attenuation correction in PET/MR. Magn Reson Mater Phys Biol Med. 2013;26(1):81–98. https://doi.org/10.1007/s10334-012-0334-7.
21. Samarin A, et al. PET/MR imaging of bone lesions—implications for PET quantification from imperfect attenuation correction. Eur J Nucl Med Mol Imaging. 2012;39(7):1154–60. https://doi.org/10.1007/s00259-012-2113-0.
22. Schulz V, et al. Automatic, three-segment, MR-based attenuation correction for whole-body PET/MR data. Eur J Nucl Med Mol Imaging. 2011;38(1):138–52. https://doi.org/10.1007/s00259-010-1603-1.
23. Robson PM, et al. MR/PET imaging of the cardiovascular system. JACC Cardiovasc Imaging.

2017;10(10 Part A):1165–79. https://doi.org/10.1016/j.jcmg.2017.07.008.
24. Ouyang J, Chun SY, Petibon Y, Bonab AA, Alpert N, El Fakhri G. Bias atlases for segmentation-based PET attenuation correction using PET-CT and MR. IEEE Trans Nucl Sci. 2013;60(5):3373–82. https://doi.org/10.1109/TNS.2013.2278624.
25. Sekine T, et al. Clinical evaluation of zero-Echo-time attenuation correction for brain ^{18}F-FDG PET/MRI: comparison with atlas attenuation correction. J Nucl Med. 2016;57(12):1927–32. https://doi.org/10.2967/jnumed.116.175398.
26. Cabello J, Lukas M, Förster S, Pyka T, Nekolla SG, Ziegler SI. MR-based attenuation correction using ultrashort-Echo-time pulse sequences in dementia patients. J Nucl Med. 2015;56(3):423–9. https://doi.org/10.2967/jnumed.114.146308.
27. Juttukonda MR, et al. MR-based attenuation correction for PET/MRI neurological studies with continuous-valued attenuation coefficients for bone through a conversion from R2* to CT-Hounsfield units. Neuroimage. 2015;112:160–8. https://doi.org/10.1016/j.neuroimage.2015.03.009.
28. Han PK, et al. MR-based PET attenuation correction using a combined ultrashort echo time/multi-echo Dixon acquisition. Med Phys. 2020;47(7):3064–77. https://doi.org/10.1002/mp.14180.
29. Leynes AP, et al. Hybrid ZTE/Dixon MR-based attenuation correction for quantitative uptake estimation of pelvic lesions in PET/MRI. Med Phys. 2017;44(3):902–13. https://doi.org/10.1002/mp.12122.
30. Izquierdo-Garcia D, et al. An SPM8-based approach for attenuation correction combining segmentation and nonrigid template formation: application to simultaneous PET/MR brain imaging. J Nucl Med. 2014;55(11):1825–30. https://doi.org/10.2967/jnumed.113.136341.
31. Delso G, et al. Anatomic evaluation of 3-dimensional ultrashort-echo-time bone maps for PET/MR attenuation correction. J Nucl Med. 2014;55(5):780–5. https://doi.org/10.2967/jnumed.113.130880.
32. Hofmann M, et al. MRI-based attenuation correction for whole-body PET/MRI: quantitative evaluation of segmentation- and atlas-based methods. J Nucl Med. 2011;52(9):1392–9. https://doi.org/10.2967/jnumed.110.078949.
33. Paulus DH, et al. Whole-body PET/MR imaging: quantitative evaluation of a novel model-based MR attenuation correction method including bone. J Nucl Med. 2015;56(7):1061–6. https://doi.org/10.2967/jnumed.115.156000.
34. Ladefoged CN, et al. A multi-centre evaluation of eleven clinically feasible brain PET/MRI attenuation correction techniques using a large cohort of patients. Neuroimage. 2017;147:346–59. https://doi.org/10.1016/j.neuroimage.2016.12.010.
35. Izquierdo-Garcia D, Catana C. MR imaging–guided attenuation correction of PET data in PET/MR Imaging. PET Clin. 2016;11(2):129–49. https://doi.org/10.1016/j.cpet.2015.10.002.
36. Torrado-Carvajal A, et al. Dixon-VIBE deep learning (DIVIDE) pseudo-CT synthesis for pelvis PET/MR attenuation correction. J Nucl Med. 2019;60(3):429–35. https://doi.org/10.2967/jnumed.118.209288.
37. Leynes AP, et al. Zero-Echo-time and Dixon deep pseudo-CT (ZeDD CT): direct generation of pseudo-CT images for pelvic PET/MRI attenuation correction using deep convolutional neural networks with multiparametric MRI. J Nucl Med. 2018;59(5):852–8. https://doi.org/10.2967/jnumed.117.198051.
38. Gong K, Han PK, Johnson KA, El Fakhri G, Ma C, Li Q. Attenuation correction using deep learning and integrated UTE/multi-echo Dixon sequence: evaluation in amyloid and tau PET imaging. Eur J Nucl Med Mol Imaging. 2021;48(5):1351–61. https://doi.org/10.1007/s00259-020-05061-w.
39. Spuhler KD, Gardus J, Gao Y, DeLorenzo C, Parsey R, Huang C. Synthesis of patient-specific transmission data for PET attenuation correction for PET/MRI neuroimaging using a convolutional neural network. J Nucl Med. 2019;60(4):555–60. https://doi.org/10.2967/jnumed.118.214320.
40. Pozaruk A, et al. Augmented deep learning model for improved quantitative accuracy of MR-based PET attenuation correction in PSMA PET-MRI prostate imaging. Eur J Nucl Med Mol Imaging. 2021;48(1):9–20. https://doi.org/10.1007/s00259-020-04816-9.
41. Grafe H, et al. Evaluation of improved attenuation correction in whole-body PET/MR on patients with bone metastasis using various radiotracers. Eur J Nucl Med Mol Imaging. 2020;47(10):2269–79. https://doi.org/10.1007/s00259-020-04738-6.
42. Nuyts J, Dupont P, Stroobants S, Benninck R, Mortelmans L, Suetens P. Simultaneous maximum a posteriori reconstruction of attenuation and activity distributions from emission sinograms. IEEE Trans Med Imaging. 1999;18(5):393–403. https://doi.org/10.1109/42.774167.
43. Nuyts J, Bal G, Kehren F, Fenchel M, Michel C, Watson C. Completion of a truncated attenuation image from the attenuated PET emission data. IEEE Trans Med Imaging. 2013;32(2):237–46. https://doi.org/10.1109/TMI.2012.2220376.
44. Lindemann ME, Oehmigen M, Blumhagen JO, Gratz M, Quick HH. MR-based truncation and attenuation correction in integrated PET/MR hybrid imaging using HUGE with continuous table motion. Med Phys. 2017;44(9):4559–72. https://doi.org/10.1002/mp.12449.
45. Eldib M, Bini J, Faul DD, Oesingmann N, Tsoumpas C, Fayad ZA. Attenuation correction for magnetic resonance coils in combined PET/MR imaging. PET Clin. 2016;11(2):151–60. https://doi.org/10.1016/j.cpet.2015.10.004.
46. Kartmann R, et al. Integrated PET/MR imaging: automatic attenuation correction of flex-

ible RF coils: AC of flexible RF surface coils. Med Phys. 2013;40(8):082301. https://doi.org/10.1118/1.4812685.
47. Klein GJ, Reutter RW, Huesman RH. Four-dimensional affine registration models for respiratory-gated PET. IEEE Trans Nucl Sci. 2002;48(3):756–60.
48. Rogers WJ, et al. Quantification of and correction for left ventricular systolic long-axis shortening by magnetic resonance tissue tagging and slice isolation. Circulation. 1991;84(2):721–31.
49. Fisher M, von Schulthess G, Higgins C. Multiphasic cardiac magnetic resonance imaging: normal regional left ventricular wall thickening. Am J Roentgenol. 1985;145(1):27–30. https://doi.org/10.2214/ajr.145.1.27.
50. Gould KL, Pan T, Loghin C, Johnson NP, Guha A, Sdringola S. Frequent diagnostic errors in cardiac PET/CT due to misregistration of CT attenuation and emission PET images: a definitive analysis of causes, consequences, and corrections. J Nucl Med. 2007;48(7):1112–21.
51. Loghin C, Sdringola S, Gould KL. Common artifacts in PET myocardial perfusion images due to attenuation-emission misregistration: clinical significance, causes, and solutions. J Nucl Med. 2004;45(6):1029–39.
52. Catana C. Motion correction options in PET/MRI. Semin Nucl Med. 2015;45(3):212–23. https://doi.org/10.1053/j.semnuclmed.2015.01.001.
53. Munoz C, Kolbitsch C, Reader AJ, Marsden P, Schaeffter T, Prieto C. MR-based cardiac and respiratory motion-compensation techniques for PET-MR imaging. PET Clin. 2016;11(2):179–91. https://doi.org/10.1016/j.cpet.2015.09.004.
54. Catana C. PET/MRI: motion correction. In: Iagaru A, Hope T, Veit-Haibach P, editors. PET/MRI in oncology: current clinical applications. Cham: Springer International; 2018. p. 77–96. https://doi.org/10.1007/978-3-319-68517-5_5.
55. Lalush DS. Magnetic resonance–derived improvements in PET imaging. Magn Reson Imaging Clin. 2017;25(2):257–72. https://doi.org/10.1016/j.mric.2016.12.002.
56. Rakvongthai Y, Fakhri GE. Magnetic resonance–based motion correction for quantitative PET in simultaneous PET-MR imaging. PET Clin. 2017;12(3):321–7. https://doi.org/10.1016/j.cpet.2017.02.004.
57. Polycarpou I, Soultanidis G, Tsoumpas C. Synergistic motion compensation strategies for positron emission tomography when acquired simultaneously with magnetic resonance imaging. Philos Trans A Soc Math Phys Eng Sci. 2021;379(2204):20200207. https://doi.org/10.1098/rsta.2020.0207.
58. Catana C, et al. MRI-assisted PET motion correction for neurologic studies in an integrated MR-PET scanner. J Nucl Med. 2011;52(1):154–61.
59. Huang C, et al. Motion compensation for brain PET imaging using wireless MR active markers in simultaneous PET-MR: phantom and non-human primate studies. Neuroimage. 2014;91:129–37.
60. Chun SY, et al. MRI-based nonrigid motion correction in simultaneous PET/MRI. J Nucl Med. 2012;53(8):1284–91.
61. Guerin B, et al. Nonrigid PET motion compensation in the lower abdomen using simultaneous tagged-MRI and PET imaging. Med Phys. 2011;38:3025.
62. Furst S, et al. Motion correction strategies for integrated PET/MR. J Nucl Med. 2015;56(2):261–9.
63. Petibon Y, et al. Relative role of motion and PSF compensation in whole-body oncologic PET-MR imaging. Med Phys. 2014;41(4):042503. https://doi.org/10.1118/1.4868458.
64. Petibon Y, et al. Impact of motion and partial volume effects correction on PET myocardial perfusion imaging using simultaneous PET-MR. Phys Med Biol. 2016;62(2):326.
65. Rank CM, et al. Respiratory motion compensation for simultaneous PET/MR based on highly undersampled MR data. Med Phys. 2016;43(12):6234–45. https://doi.org/10.1118/1.4966128.
66. Fuin N, et al. Concurrent respiratory motion correction of abdominal PET and dynamic contrast-enhanced–MRI using a compressed sensing approach. J Nucl Med. 2018;59(9):1474–9. https://doi.org/10.2967/jnumed.117.203943.
67. Dutta J, Huang C, Li Q, El Fakhri G. Pulmonary imaging using respiratory motion compensated simultaneous PET/MR. Med Phys. 2015;42(7):4227–40.
68. Fayad H, Schmidt H, Wuerslin C, Visvikis D. Reconstruction-incorporated respiratory motion correction in clinical simultaneous PET/MR imaging for oncology applications. J Nucl Med. 2015;56(6):884–9.
69. Grimm R, et al. Self-gated MRI motion modeling for respiratory motion compensation in integrated PET/MRI. Med Image Anal. 2015;19(1):110–20.
70. Wang X, Rahmim A, Tang J. MRI-assisted dual motion correction for myocardial perfusion defect detection in PET imaging. Med Phys. 2017;44(9):4536–47. https://doi.org/10.1002/mp.12429.
71. Petibon Y, et al. Cardiac motion compensation and resolution modeling in simultaneous PET-MR: a cardiac lesion detection study. Phys Med Biol. 2013;58(7):2085–102. https://doi.org/10.1088/0031-9155/58/7/2085.
72. Küstner T, et al. MR-based respiratory and cardiac motion correction for PET imaging. Med Image Anal. 2017;42:129–44. https://doi.org/10.1016/j.media.2017.08.002.
73. Huang C, et al. Accelerated acquisition of tagged MRI for cardiac motion correction in simultaneous PET-MR: phantom and patient studies. Med Phys. 2015;42(2):1087–97.
74. Robson PM, et al. Correction of respiratory and cardiac motion in cardiac PET/MR using MR-based motion modeling. Phys Med Biol. 2018;63(22):225011. https://doi.org/10.1088/1361-6560/aaea97.

75. Kolbitsch C, et al. Cardiac and respiratory motion correction for simultaneous cardiac PET/MR. J Nucl Med. 2017;58(5):846–52. https://doi.org/10.2967/jnumed.115.171728.
76. Petibon Y, El Fakhri G, Nezafat R, Johnson N, Brady T, Ouyang J. Towards coronary plaque imaging using simultaneous PET-MR: a simulation study. Phys Med Biol. 2014;59(5):1203–22. https://doi.org/10.1088/0031-9155/59/5/1203.
77. Munoz C, et al. Motion-corrected simultaneous cardiac positron emission tomography and coronary MR angiography with high acquisition efficiency. Magn Reson Med. 2018;79(1):339–50. https://doi.org/10.1002/mrm.26690.
78. Munoz C, Neji R, Kunze KP, Nekolla SG, Botnar RM, Prieto C. Respiratory- and cardiac motion-corrected simultaneous whole-heart PET and dual phase coronary MR angiography. Magn Reson Med. 2019;81(3):1671–84. https://doi.org/10.1002/mrm.27517.
79. Mayer J, Jin Y, Wurster T-H, Makowski MR, Kolbitsch C. Evaluation of synergistic image registration for motion-corrected coronary NaF-PET-MR. Philos Trans A Soc Math Phys Eng Sci. 2021;379(2200):20200202. https://doi.org/10.1098/rsta.2020.0202.
80. Axel L, Dougherty L. MR imaging of motion with spatial modulation of magnetization. Radiology. 1989;171(3):841–5. https://doi.org/10.1148/radiology.171.3.2717762.
81. Petibon Y, Sun T, Han PK, Ma C, Fakhri GE, Ouyang J. MR-based cardiac and respiratory motion correction of PET: application to static and dynamic cardiac ^{18}F-FDG imaging. Phys Med Biol. 2019;64(19):195009. https://doi.org/10.1088/1361-6560/ab39c2.
82. Petibon Y, et al. Impact of motion and partial volume effects correction on PET myocardial perfusion imaging using simultaneous PET-MR. Phys Med Biol. 2017;62(2):326–43. https://doi.org/10.1088/1361-6560/aa5087.
83. Würslin C, et al. Respiratory motion correction in oncologic PET using T1-weighted MR imaging on a simultaneous whole-body PET/MR system. J Nucl Med. 2013;54(3):464–71. https://doi.org/10.2967/jnumed.112.105296.
84. Büther F, et al. List mode-driven cardiac and respiratory gating in pet. J Nucl Med. 2009;50(5):674–81.
85. Qiao F, Pan TS, Clark JWJ, Mawlawi OR. A motion-incorporated reconstruction method for gated PET studies. Phys Med Biol. 2006;51:3769–83.
86. Lamare F, et al. List-mode-based reconstruction for respiratory motion correction in PET using non-rigid body transformations. Phys Med Biol. 2007;52(17):5187–204. https://doi.org/10.1088/0031-9155/52/17/006.
87. Nekolla SG, et al. Evaluation of the novel myocardial perfusion positron-emission tomography tracer ^{18}F-BMS-747158-02: comparison to ^{13}N-ammonia and validation with microspheres in a pig model. Circulation. 2009;119(17):2333–42. https://doi.org/10.1161/CIRCULATIONAHA.108.797761.
88. Marin T, et al. Motion correction for PET data using subspace-based real-time MR imaging in simultaneous PET/MR. Phys Med Biol. 2020;65(23):235022. https://doi.org/10.1088/1361-6560/abb31d.
89. Spangler-Bickell MG, Deller TW, Bettinardi V, Jansen F. Ultra-fast list-mode reconstruction of short PET frames and example applications. J Nucl Med. 2021;62(2):287–92. https://doi.org/10.2967/jnumed.120.245597.
90. Lu Y, et al. Data-driven voluntary body motion detection and non-rigid event-by-event correction for static and dynamic PET. Phys Med Biol. 2019;64(6):065002. https://doi.org/10.1088/1361-6560/ab02c2.
91. Sun T, et al. Body motion detection and correction in cardiac PET: phantom and human studies. Med Phys. 2019;46(11):4898–906. https://doi.org/10.1002/mp.13815.
92. Martin O, et al. PET/MRI versus PET/CT for whole-body staging: results from a single-center observational study on 1,003 sequential examinations. J Nucl Med. 2020;61(8):1131–6. https://doi.org/10.2967/jnumed.119.233940.
93. Sher AC, et al. Assessment of sequential PET/MRI in comparison with PET/CT of pediatric lymphoma: a prospective study. Am J Roentgenol. 2016;206(3):623–31. https://doi.org/10.2214/AJR.15.15083.
94. Gatidis S, Bender B, Reimold M, Schäfer JF. PET/MRI in children. Eur J Radiol. 2017;94:A64–70. https://doi.org/10.1016/j.ejrad.2017.01.018.
95. Moradi F, Iagaru A, McConathy J. Clinical applications of PET/MR imaging. Radiol Clin North Am. 2021;59(5):853–74. https://doi.org/10.1016/j.rcl.2021.05.013.
96. Pearce MS, et al. Radiation exposure from CT scans in childhood and subsequent risk of leukaemia and brain tumours: a retrospective cohort study. Lancet. 2012;380(9840):499–505. https://doi.org/10.1016/S0140-6736(12)60815-0.
97. On behalf of the European Society of Cardiovascular Radiology (ESCR), et al. Hybrid cardiac imaging using PET/MRI: a joint position statement by the European Society of Cardiovascular Radiology (ESCR) and the European Association of Nuclear Medicine (EANM). Eur J Hybrid Imaging. 2018;2(1):4086–101. https://doi.org/10.1186/s41824-018-0032-4.
98. Messroghli DR, et al. Clinical recommendations for cardiovascular magnetic resonance mapping of T1, T2, T2 and extracellular volume: a consensus statement by the Society for Cardiovascular Magnetic Resonance (SCMR) endorsed by the European Association for Cardiovascular Imaging (EACVI). J Cardiovasc Magn Reson. 2017;19(1):1–24. https://doi.org/10.1186/s12968-017-0389-8.

99. Messroghli DR, Radjenovic A, Kozerke S, Higgins DM, Sivananthan MU, Ridgway JP. Modified look-locker inversion recovery (MOLLI) for high-resolution T 1 mapping of the heart. Magn Reson Med. 2004;52(1):141–6. https://doi.org/10.1002/mrm.20110.
100. Kellman P, Hansen MS. T1-mapping in the heart: accuracy and precision. J Cardiovasc Magn Reson. 2014;16(2):1–20.
101. Verhaert D, et al. Direct T2 quantification of myocardial edema in acute ischemic injury. JACC Cardiovasc Imaging. 2011;4(3):269–78. https://doi.org/10.1016/j.jcmg.2010.09.023.
102. Kramer CM, Barkhausen J, Bucciarelli-Ducci C, Flamm SD, Kim RJ, Nagel E. Standardized cardiovascular magnetic resonance imaging (CMR) protocols: 2020 update. J Cardiovasc Magn Reson. 2020;22(1):17. https://doi.org/10.1186/s12968-020-00607-1.
103. Sung K, Nayak KS. Measurement and characterization of RF nonuniformity over the heart at 3T using body coil transmission. J Magn Reson Imaging. 2008;27(3):643–8. https://doi.org/10.1002/jmri.21253.
104. Weingärtner S, Roujol S, Akçakaya M, Basha TA, Nezafat R. Free-breathing multislice native myocardial T1 mapping using the slice-interleaved T1 (STONE) sequence. Magn Reson Med. 2015;74(1):115–24. https://doi.org/10.1002/mrm.25387.
105. Qi H, et al. Free-running 3D whole heart myocardial T1 mapping with isotropic spatial resolution. Magn Reson Med. 2019;82(4):1331–42. https://doi.org/10.1002/mrm.27811.
106. Han PK, et al. Free-breathing 3D cardiac T_1 mapping with transmit B_1 correction at 3T. Magn Reson Med. 2021;87(4):1832–45. https://doi.org/10.1002/mrm.29097.
107. Shaw JL, et al. Free-breathing, non-ECG, continuous myocardial T1 mapping with cardiovascular magnetic resonance multitasking. Magn Reson Med. 2019;81(4):2450–63. https://doi.org/10.1002/mrm.27574.
108. Hamilton JI, Jiang Y, Eck B, Griswold M, Seiberlich N. Cardiac cine magnetic resonance fingerprinting for combined ejection fraction, T1 and T2 quantification. NMR Biomed. 2020;33(8):1–17. https://doi.org/10.1002/nbm.4323.